Iraqi Journal of Physics, 2024 *Vol. 22, No. 1, PP.82-94*

https://doi.org/10.30723/ijp.v22i1.1212

P-ISSN: 2070-4003
E-ISSN: 2664-5548

Preparation and Study the Properties of PVDF/PEO/WO_2 Hybrid Nanocomposite Thin Films Prepared by a Spin Coating Method

Aseel N. Bardan [1a]* and Lamia K. Abbas [1b]
[1]*Department of Physics, College of Science, University of Baghdad, Baghdad, Iraq*
[b]E-mail: dr.lamia.abbas@gmail.com
[a*]Corresponding author: asoaldulaymi@gmail.com

Abstract

In this work, using the spin coating method to create polyvinylidene fluoride (PVDF)/polyethylene oxide (PEO) thin films, the effects of nano-tungsten oxide (WO_2) doping were investigated. The novelty of this research lies in its investigation of varying weight concentrations of WO_2 nanoparticles (NPs) within the composite films. Comprehensive characterization techniques were employed, including structural analysis via X-ray diffraction (XRD), which revealed a clear and prominent peak in the XRD of the PVDF/PEO films, and the films' polycrystalline nature with tetragonal structures. The grain size was noted to increase with higher WO_2 NPs doping. Field emission scanning electron microscopy (FE-SEM) showed hexagonal-like α-phase PVDF crystals and uniform distribution of WO_2 NPs. Furthermore, Fourier-transform infrared spectroscopy (FTIR) confirmed the characteristics of PVDF/PEO and identified specific doping compounds, confirming successful incorporation. The optical transmittance spectra unveiled the films' optical band gap energy, optical transition types, and absorption characteristics, where novelty emerged as the band gap energy significantly increased from 3.0 eV to 3.64 eV with an increased WO_2 NPs weight doping percentage, signifying profound electronic structure modifications and potential applications in optoelectronics and sensors.

Article Info.

Keywords:
PVDF/PEO, Nanocomposite, Spin Coating, Polycrystalline, FE-SEM.

Article history:
Received: Oct. 10, 2023
Revised: Dec. 10, 2023
Accepted: Dec.21, 2023
Published: Mar. 01,2024

1. Introduction

Polymers are cross-linked monomers or small molecules arranged into repeating basic units. The formation of these entities leads to various products, each with distinct characteristics [1-3]. Extensive research is being conducted on polymer thin films, focusing mainly on their applications in various fields, including sensors, microelectronics, energy technologies, optics, medicine, and biotechnology [4-8]. Polyvinylidene fluoride (PVDF) is a polymer with unique properties, such as electroactivity, piezoelectricity, and biocompatibility. Due to its inherent properties, this material has promising potential for various applications, including sensors, actuators, energy harvesting devices, battery separators, and filtration membranes [9-14]. Polyethylene oxide (PEO), is a polyether with elastic properties, is devoid of toxicity, and is water soluble. It has been used in many sectors, such as cosmetics, food processing, and medicinal preparations. PEO has garnered significant scientific interest in its use as a polymer electrolyte. It functions as a reliable solvent for salts, particularly lithium salts, facilitating the movement of ions in the solid state. Solid polymer electrolytes based on PEO have several benefits compared to liquid organic electrolytes. These advantages include simplified production, consistent electrochemical properties, and exceptional mechanical [15-17].

Incorporating chemicals into polymers has many possible uses [18]. Comprehensive investigations dedicated to exploring the capacity of doped polymer nanocomposites to attain a homogeneous dispersion or widespread incorporation of inorganic constituents within the polymer matrix were reported by many studies [19-

21]. Incorporating inorganic nanocomposites scattered throughout the polymer matrix has numerous electronic applications, such as catalysis, organic batteries, electronics, and optoelectronics [22, 23]. Tungsten oxide (WO_3) is an n-type semiconductor with a reported band gap within the approximate range of 2.6 to 2.8 eV [24, 25]. The intrinsic conductivity of the material is a consequence of its non-stoichiometric composition, which creates a donor level due to the presence of oxygen vacancy defects within the lattice structure [26]. The tungsten compound exhibits several forms due to its ability to exist in different oxidation states, including 2, 3, 4, 5, and 6. Two common types of tungsten oxides are tungsten (VI) oxide (WO_3), which exhibits a lemon yellow colour, and tungsten (IV) oxide (WO_2), which displays a brown and blue appearance [27]. The vast range of uses for tungsten oxides may be attributed to their favourable electrical characteristics. These qualities render them appropriate for electrochromic devices, photochromic materials, photocatalysts, and gas sensors [28, 29].

This work examines the effect of doping different WO_2 weight ratios on the morphological, optical, and structural properties of PVDF/PEO films. The investigation included the use of characterization methods, namely X-ray diffraction (XRD), Fourier-transform infrared spectroscopy (FTIR), and ultraviolet-visible spectrometry (UV-vis).

2. Experimental Work

For this work, polymer powders were purchased from Sigma-Aldrich and Merck KGaA, Darmstadt, Germany. Polyethylene Oxide (PEO, with a density range of 1.11–1.2 kg/liter) and Poly Vinylidene Fluoride (PVDF, with an average molecular weight of 534,000) were mixed, such that PVDF comprised 75% (0.75 g) of the total weight and PEO 25% (0.25 g). The polymer mixture was dissolved in 20 ml of a 99.98% pure Dimethylformamide (DMF) solvent to obtain a homogenous solution. The solution was agitated continuously at 65°C for around one hour. Tungsten oxide (WO_2) nanoparticles (obtained from Sky Spring Nanomaterials, Inc.) were used for doping at 5, 10, 15, and 20% doping percentages. WO_2 NPs were dissolved in 20 ml of DMF and added to the PVDF/PEO solution. This solution was continuously stirred for 4 hrs at 65°C until homogeneity was reached. The spin coating technology was then used to create nanocomposite films. The solution was deposited onto 2.5 × 2.5 cm glass substrates using a ToosNano Spin Coater (SPC-TN-556).

The final films were examined for crystal structure with an X-ray diffractmeter (XRD) (Panalytical X′ Pert Pro). A field-emission scanning electron microscope (FE-SEM) (JSM-7600 F, made by JEOL Ltd., Japan) was used to analyze the thin films' microstructure. Before analysis, the films were coated with a layer of gold. The functional groups and bonds present in the samples were examined with a Fourier-transform infrared (FTIR) spectrometer (Shimadzu FTIR-1800). The optical energy gap of each produced sample was measured during optical inspections. At room temperature, the optical transmittance and absorption spectra of the PVDF/PEO/WO_2 nanocomposite thin films were measured with a UV-visible spectrophotometer (Shimadzu UV-visible UV160A).

3. Results and Discussion

3.1. X-Ray Diffraction Analysis

XRD analysis was employed to investigate the crystal structure of pristine PVDF/ PEO thin films with a weight ratio of 75/25, and PVDF/PEO doped with WO_2 at different doping percentages. The XRD patterns of PVDF/PEO and PVDF/PEO/WO_2 thin films are depicted in Fig. 1. The diffraction patterns exhibited several peaks, indicating that the produced films possessed a polycrystalline structure. A clear and prominent peak was seen in the XRD pattern of the PVDF/PEO thin film at 2θ angles of

20.237° and 16.7°, corresponding to the crystallographic planes (110) and (020), respectively. Following doping, a noticeable displacement of the peak's position towards higher values of 2θ was noted. Also, new peaks at the angles 25.8°, 36.9°, 37.5°, 52.9°, 53.6°, and 59.8°, were noted. These peaks correspond to the crystallographic planes (110), (200), (101), (220), (111), and (310), respectively.

Furthermore, it was seen that the intensity of these newly emerged peaks increased in correspondence with the doping ratios of WO_2, providing evidence in favor of improving the crystal structure [30, 31]. The amount of crystallinity attained may be inferred by the degree of sharpness displayed by the peaks. The average crystal size (D) was determined using Scherer's formula [32]:

$$D = \frac{k\lambda}{\beta \cos\theta} \quad (1)$$

where: D is crystallite size, k (=0.94) is shape factor, λ (=0.154 nm) is the wavelength of radiation, β is the full width half maximum and θ is the position of the peak The average crystal size of the PVDF/PEO composite material was found to be 14.3 nm. As the doping concentration of PVDF/PEO increased from 5% to 20%, the average crystal size increased from 14.75 nm to 18.46 nm. Additionally, an enhancement in the structural characteristics of the generated films was noted in response to the increase in the average crystal size [33]. Table 1 displays the XRD peaks intensities and the crystallite size of all samples.

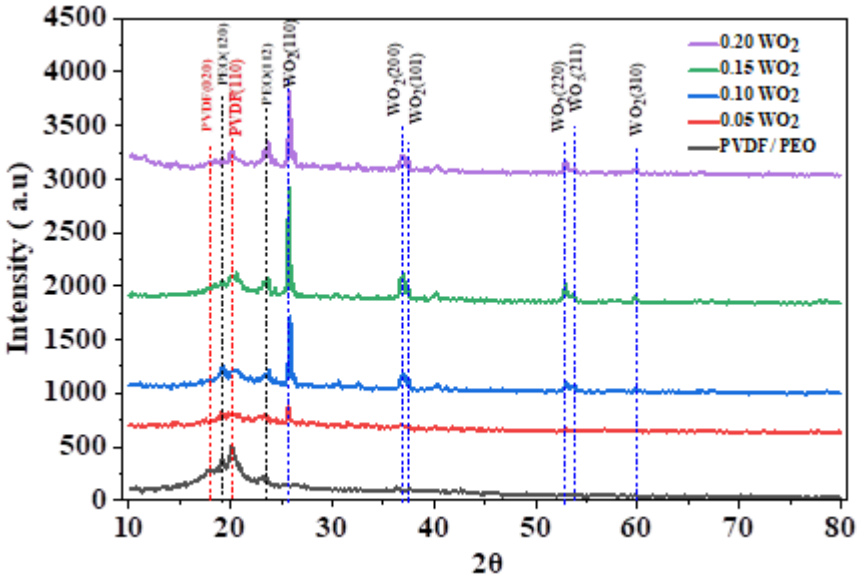

Figure 1: XRD patterns of PVDF/PEO and PVDF/PEO/WO_2 thin films at various doping concentrations (5, 10, 15, and 20%).

Table 1: XRD peak intensities of all samples.

Sample	2θ (Deg.)	FWHM (Deg.)	d_{hkl} Exp.(Å)	D (nm)	hkl	Phase
PVDF/ PEO	17.9302	0.7107	4.9431	11.3	(020)	PVDF
	19.1646	0.4863	4.6274	16.6	(120)	PEO
	20.0998	0.4863	4.4142	16.6	(110)	PVDF
	23.4663	0.6359	3.7880	12.8	(112)	PEO
0.05 WO_2	19.1445	0.5162	4.6322	15.6	(120)	PEO
	20.1770	1.1062	4.3975	7.3	(110)	PVDF
	23.3481	0.9218	3.8069	8.8	(112)	PEO
	25.6711	0.3319	3.4674	24.5	(110)	WO_2
	36.8805	0.5531	2.4352	15.1	(200)	WO_2
	52.8466	0.5162	1.7310	17.2	(220)	WO_2
0.10 WO_2	19.1814	0.4056	4.6234	19.9	(120)	PEO
	20.5088	0.9956	4.3271	8.1	(110)	PVDF
	23.4587	0.5531	3.7892	14.7	(112)	PEO
	25.8555	0.2581	3.4431	31.6	(110)	WO_2
	36.9912	0.5900	2.4282	14.2	(200)	WO_2
	37.5811	0.2581	2.3914	32.5	(101)	WO_2
	52.9941	0.4056	1.7265	21.9	(220)	WO_2
	53.6578	0.5162	1.7067	17.2	(111)	WO_2
	59.8156	0.6268	1.5449	14.6	(310)	WO_2
0.15 WO_2	19.2183	0.4056	4.6146	19.9	(120)	PEO
	20.2507	0.9587	4.3816	8.4	(110)	PVDF
	23.4956	0.7006	3.7833	11.6	(112)	PEO
	25.7817	0.2582	3.4528	31.6	(110)	WO_2
	36.8437	0.5900	2.4376	14.2	(200)	WO_2
	37.4336	0.3688	2.4005	22.7	(101)	WO_2
	52.9572	0.4056	1.7277	21.9	(220)	WO_2
	53.7316	0.4425	1.7046	20.1	(111)	WO_2
	59.7419	0.5162	1.5466	17.7	(310)	WO_2
0.20 WO_2	19.1814	0.4056	4.6234	19.9	(120)	PEO
	20.1770	0.5531	4.3975	14.6	(110)	PVDF
	23.4587	0.7006	3.7892	11.6	(112)	PEO
	25.7448	0.3318	3.4577	24.6	(110)	WO_2
	36.9174	0.5531	2.4329	15.1	(200)	WO_2
	37.5811	0.4425	2.3914	19.0	(101)	WO_2
	52.9572	0.3318	1.7277	26.7	(220)	WO_2
	53.8422	0.4425	1.7013	20.1	(111)	WO_2
	59.8156	0.6269	1.5449	14.6	(310)	WO_2

3.2. Surface Morphology

The investigation was conducted with a FE-SEM at various scales and magnification levels. Fig. 2 illustrates the FE-SEM micrographs of PVDF/PEO; it shows the existence of hexagonal-like α-phase PVDF crystals, which have a fibrous structure resembling miniature fibers [33, 34]. The viscosity of PEO is noteworthy. The microscopic photos presented in Figs. 2-6 depict the pure PVDF/PEO sample as well as samples of different WO_2 nanoparticles doping concentration (5, 10, 15, and 20%). The figures illustrate the effects of including WO_2 nanoparticles in the PVDF/PMMA composite. It shows the existence of many spherical nanoparticles, the formation of a rough surface, and increased porosity, which increased hydrophilicity. These images provide evidence of a direct relationship between the doping percentages of WO_2 nanoparticles and the observed enlargement in pore size. Based on the findings in Figs 5 and 6, a direct correlation is observed between the proportion of tungsten oxide in the substance and the concurrent rise in porosity.

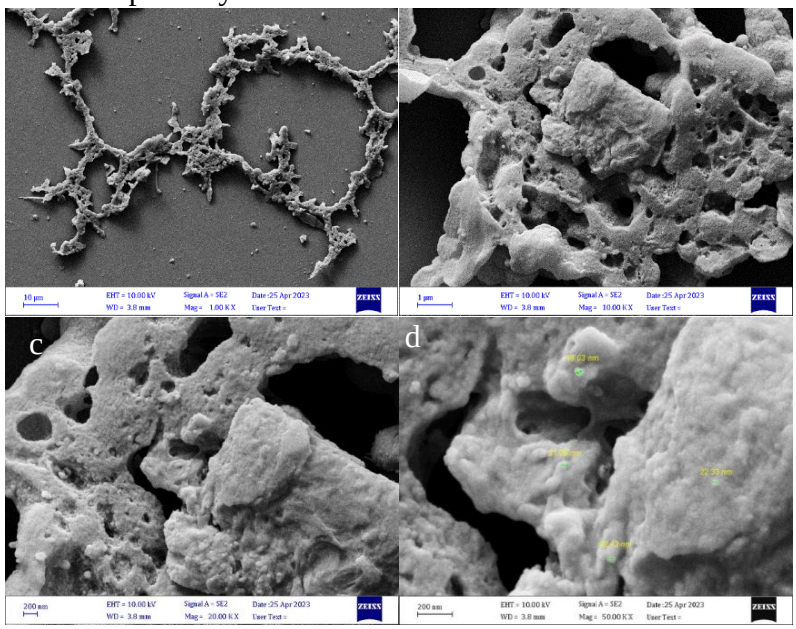

Figure 2: FE-SEM micrographs (a, b, c and d) of PVDF/ PEO.

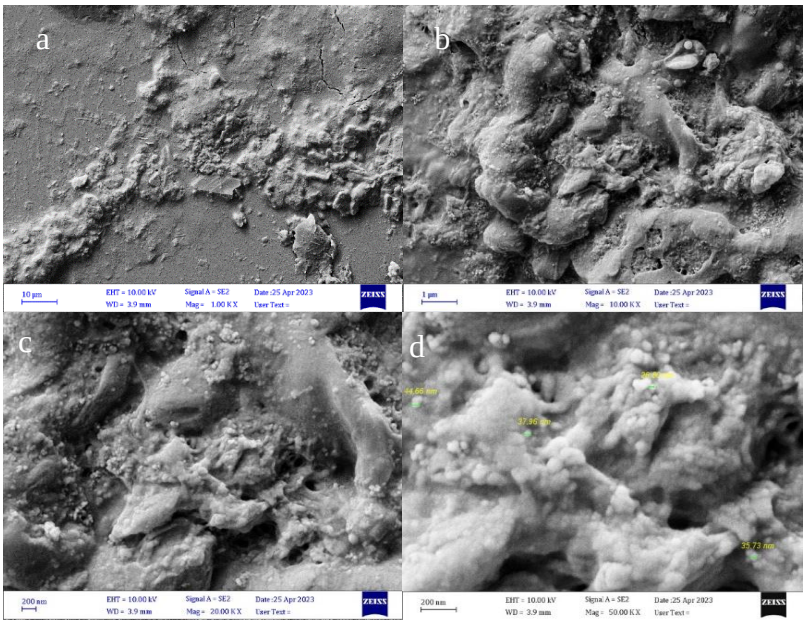

Figure 3: FE-SEM micrographs of 5 % (a, b, c and d) PVDF/PEO/ WO_2.

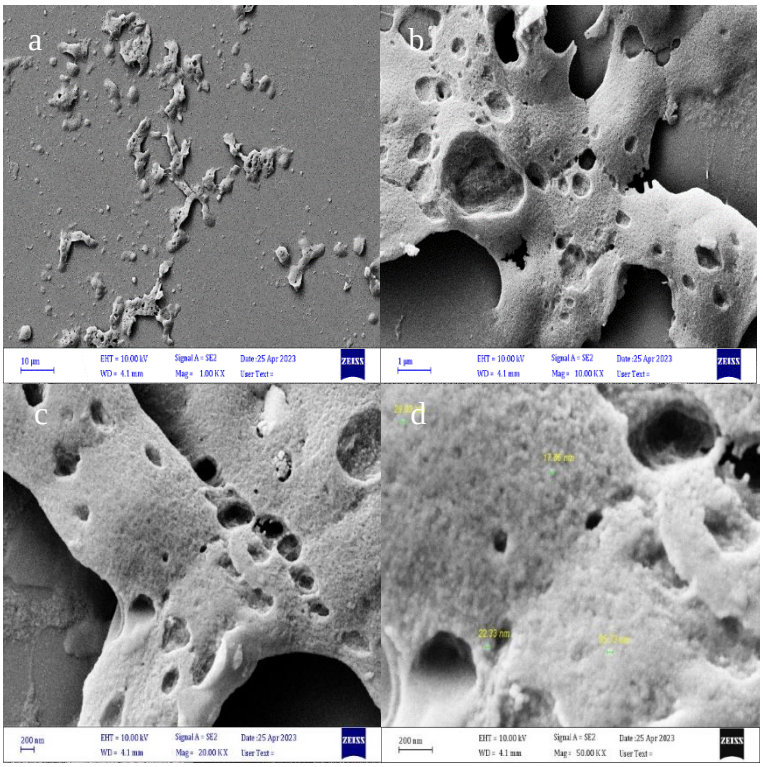

Figure 4: FE-SEM micrographs of 10 %(a, b, c and d) PVDF/PEO/ WO2.

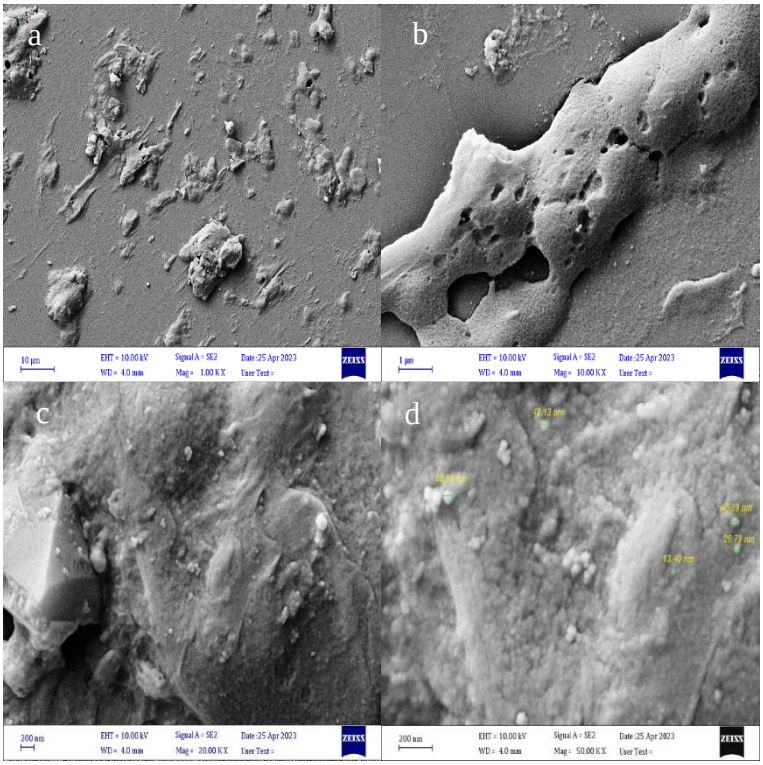

Figure 5: FE-SEM micrographs of 15 %(a, b, c and d) PVDF/PEO/ WO2.

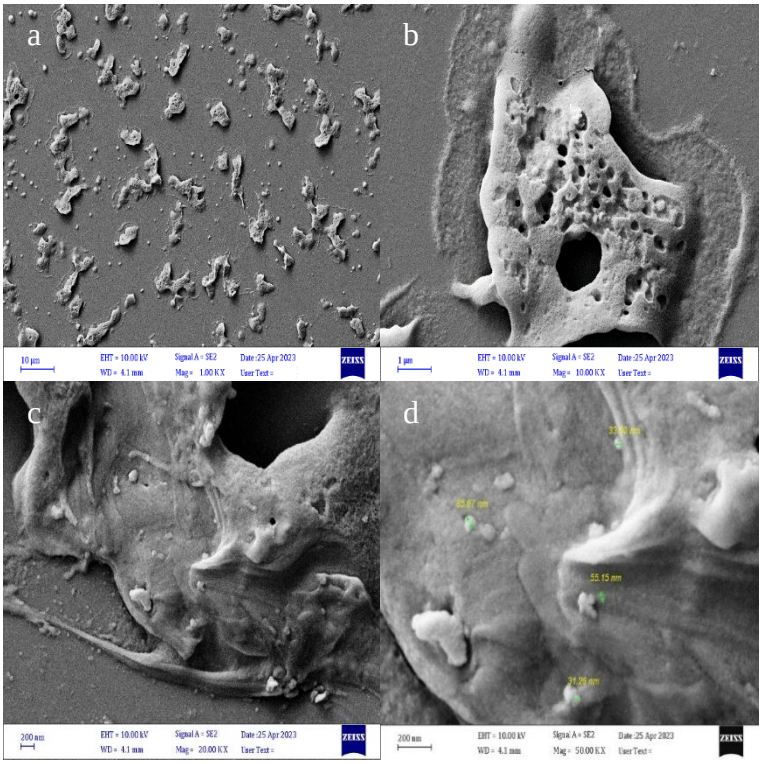

Figure 6: FE-SEM micrographs of 20 %(a, b, c and d) PVDF/PEO/ WO2.3.3.

3.3. EDX Analysis

Energy dispersive X-ray (EDX) analysis was used to ascertain the chemical composition of PVDF/PEO and PVDF/PEO/WO_2 nanocomposites with different WO_2 nanoparticles doping percentages (5, 10, 15, and 20%, as shown in Fig. 7. The EDX spectra of PVDF/PEO/WO_2 revealed the existence of WO_2 nanoparticles inside the PVDF/PEO composite. The concentration levels obtained from the study exhibited a percentage of error, indicating deviations from the expected values, both in terms of decline and rise. These deviations were considered less than desirable. The study indicated that the spectra mentioned above are composed of tungsten (W) and oxide (O) produced from the WO_2 structure, together with carbon and oxide emerging from the PVDF/PEO structure [35].

3.4. FT-IR Spectroscopy

FT-IR spectroscopy is an essential technique for identifying chemical bond functional groups, owing to its utilization of the unique infrared radiation absorption shown by these groups in their vibrational modes [36]. Fig. 8 displays the FTIR spectra of PVDF/PEO and PVDF/PEO/WO_2 nanocomposite thin films with different doping percentages (5, 10, 15, and 20%) at 960 and 842 cm^{-1} wavenumbers. The samples bands include the spectral range of the nanocomposites (PVDF/PEO)/WO_2 and (PVDF/PEO)/PEO. According to the data shown in Fig. 4, it can be seen that PVDF exhibits three different polymorphic phases, each with a distinctive arrangement of spectral bands. The existence of WO_2 nanoparticles in the PVDF/PEO/WO_2 nanocomposite spectra is verified by detecting a spectral band at 601 cm^{-1}, indicative of the W-O stretching vibration, which is absent in the spectra of PVDF/PEO [37]. In both the PVDF/PEO and PVDF/PEO/WO_2 nanocomposites, the crystalline α-phase of PVDF is identified by a specific band within the (840-879) cm^{-1} range, while a band represents the crystalline β-phase at around 879.2 cm^{-1} [37-40].

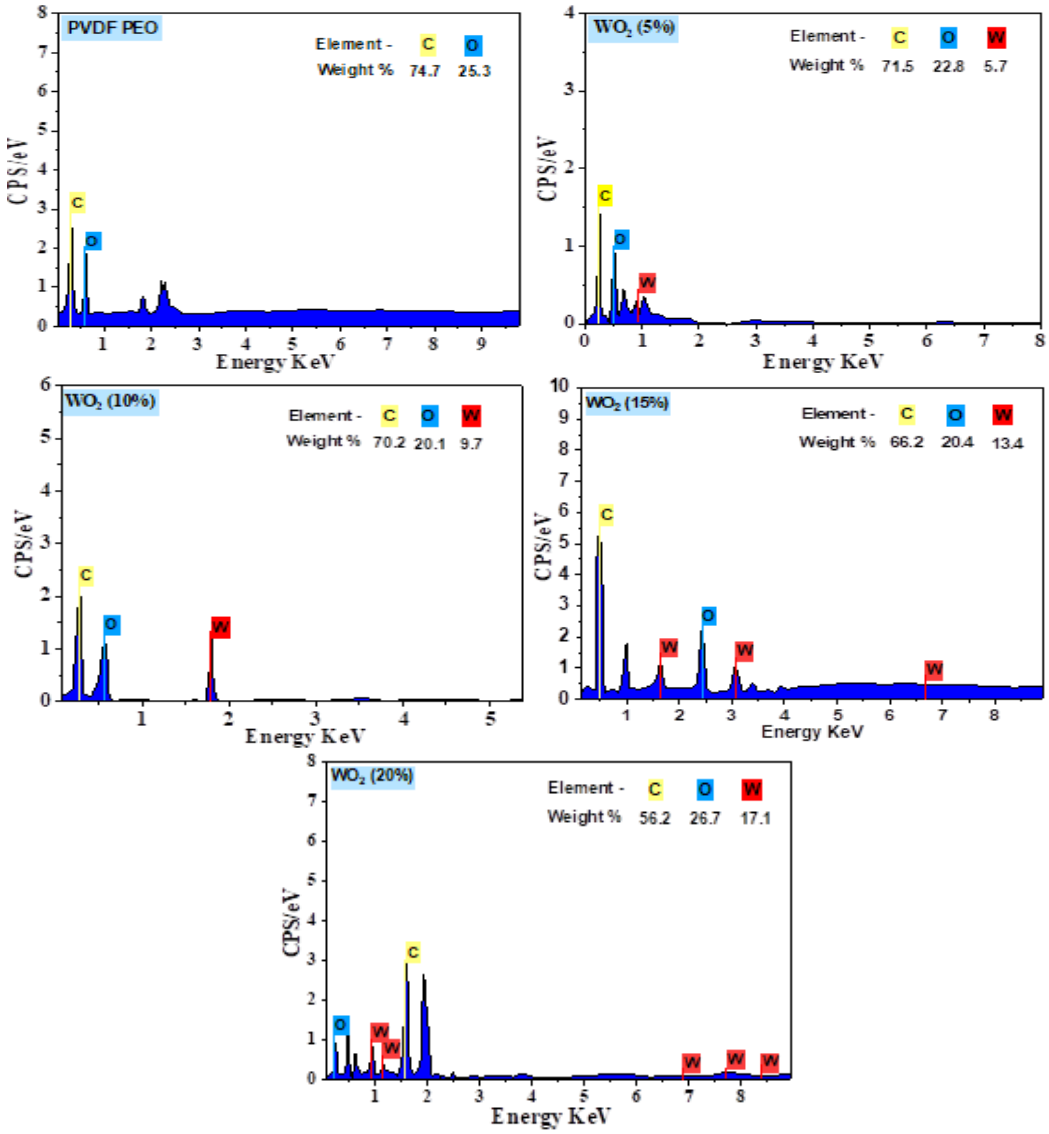

Figure 7: EDX spectra of a PVDF/ PEO and PVDF/PEO/ WO_2 at different doping percentages (5, 10, 15 and 20 %).

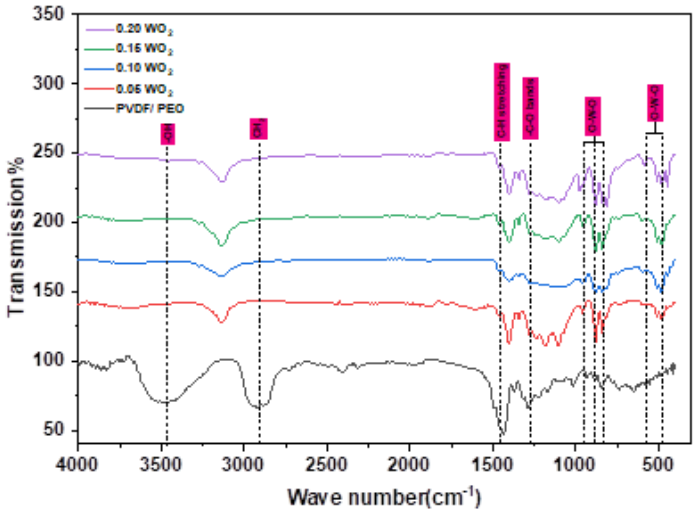

Figure 8: FTIR analysis of PVDF/PEO and (PVDF/PEO)/WO_2 nanocomposite thin films at ambient conditions.

Furthermore, the distinctive characteristic of PEO is the peak at 1650.54 cm^{-1}, which may be attributed to the carbonyl group (C-O). An additional band seen at 1186 cm^{-1} suggests the occurrence of a stretching vibration related to surface hydroxyl groups or adsorbed water. This phenomenon is likely attributed to the re-adsorption of water from the ambient environment. The observed bands at 1436.14 cm^{-1} and 1290.16 cm^{-1}, which align with the tungsten-hydroxyl (W-OH) vibrations, are ascribed to the presence of hydroxyl groups (C-H) [41].

3.5. Optical Properties

Fig. 9 displays the UV absorbance spectra of thin films of PVDF/PEO and PVDF/PEO/WO_2 nanocomposites of different doping percentages of WO_2 NPs (5, 10, 15, and 20wt. %). The optical characteristics of PVDF/PEO and PVDF/PEO/WO_2 nanocomposite thin films were evaluated using UV-visible spectroscopy throughout 200-1100 nm wavelength range under average temperature conditions. As can be observed from the figure, the absorbance spectra experience a downward trend with the increase of the WO_2 NPs doping percentage. The absorbance spectrum of the PVDF/PEO thin film revealed that the visible region exhibited a significant absorption level, as previously mentioned. However, the absorbance values decreased when 5% and 10% by weight of WO_2 NPs were added to the PVDF/PEO group, the absorbance decreased further with the increase of WO_2 NPs ratio. There is a possibility that the light scattering is reduced due to the diffusion of WO_2 molecules through the polymer chains, which also has the potential to lower the density and the molecular weight. Doping the material with WO_2 NPs of varied weight ratios reduced surface roughness, which might be explained by the above finding [42, 43]. In addition, the absorbance of the PVDF/PEO/WO_2 nanocomposite thin films showed a considerable rise in the UV region. The electronic transitions inside the band gap may explain this phenomenon.

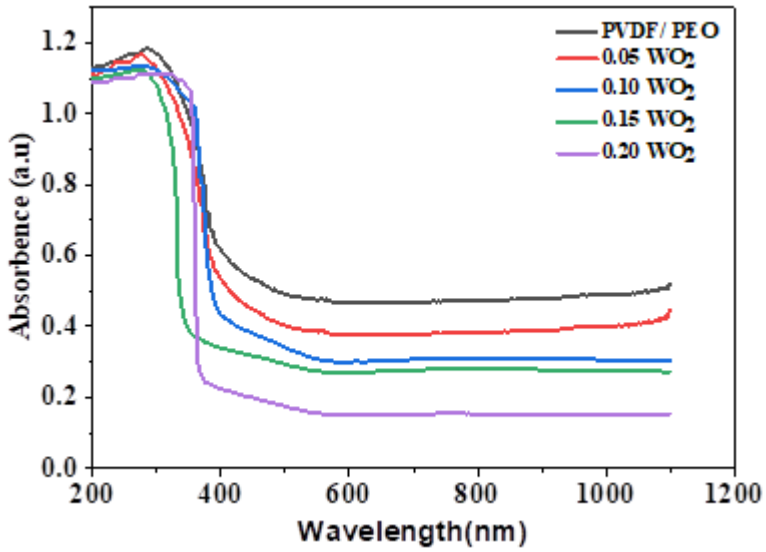

Figure 9: UV-Vis spectra of PVDF/PEO and (PVDF/PEO)/WO_2 of different doping percentages (5, 10, 15 and 20 %).

The Tauc equation was used to determine the optical energy gap (E_g) values for PVDF/PEO and PVDF/PEO/WO_2 nanocomposite thin films. Eq. (2) demonstrates how this equation may be used to compute E_g by looking at the area of high absorption that is located near the films' absorption edge [44, 45]:

$$\alpha h\nu = B(h\nu - E_g)^r \qquad (2)$$

The calculation of the optical absorption coefficient (α) encompasses several variables, such as E_g, incident photon energy (hν) measured in electron volts (eV), material structure (B), and the index (r) that characterizes the optical absorption process, as delineated by eq. 2 [46, 47]. This relationship exhibits a linear dependence, suggesting the presence of permissible direct transitions. Consequently, the extrapolation of the relationship of $(\alpha h\nu)^2$ against the Tauc plot for pure PVDF/PEO. The dissimilarity of $(\alpha h\nu)^2$ as a function of (hν) is depicted in (hν) at α= 0 is employed to ascertain the value of E_g, as illustrated in Fig. 10, which presents the plot for thin films of PVDF/PEO/WO_2 nanocomposites with varying weight doping concentration (5, 10, 15, and 20 wt.% of WO_2 NPs) shown in Fig. 10. It has been determined that the optical energy gap of PVDF/PEO is 3.0 eV. The values of the optical energy gap of PVDF/PEO/WO2 of WO_2 NPs doping ratios (5, 10, 15, and 20 wt.%) were 3.086, 3.22, 3.44, and 3.64 eV, respectively. As the weight ratio of WO_2 NPs rises, an increase in the PVDF/composite films' optical energy gap may be seen. Previous studies have shown that the interaction between WO_2 nanoparticles and the polymer matrix may result in flaws in the structure and macrostrains connected to higher PVDF/PMMA's optical energy gap values [48]. The increase in the band gap's density of localized states is partly caused by disordered defects and by stresses of a very minor magnitude [49]. The energy gap increased with the increase of doping due to the extended localization arising from the poor crystallinity [50].

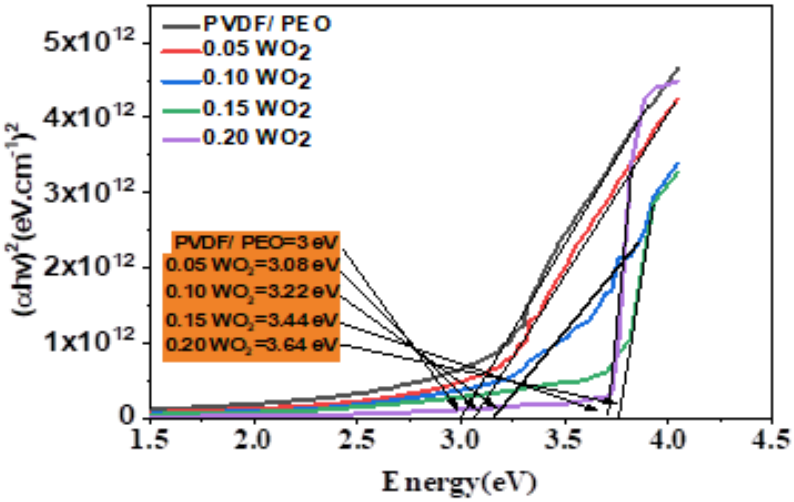

Figure 10: Tauc's plot for thin films made of pure PVDF/PEO and PVDF/PEO/WO_2 NPs nanocomposites with varying weight ratios (5 ,10, 15 and 20%) of WO_2 NPs.

3.6. Hall Effect Measurements

Hall measurements were employed to investigate how altering the weight doping concentration of WO_2 NPs influenced both the charge carrier concentration (n_H) and the mobility of charge carriers (u_H) within the PVDF/PEO films. According to the results, there was a correlation between the amount of doping and the decrease in resistance. These data align with prior research by Basappa et al. [51], which showed that resistivity decreased as tungsten oxide concentration increased until the rising concentration reached its maximum value. More charge carriers are created when a greater doping level is present in the material. This is because there is an increased supply of atoms and a decreased number of scattering centers. In addition, the presence of oxygen vacancies boosts conductivity, which, in turn, leads to enhanced conductivity (i.e., lower resistance) when the fraction of oxygen vacancies in a material increase. Additional information on the produced films is included in Table 2, including the

carrier concentration, mobility, and sample conductivity values. The result obtained with a percentage doping of 15% was the most advantageous because it had the maximum electrical conductivity. The table illustrates relatively how increasing the fraction of tungsten oxide up to 20% that has been deposited can result in improved sample mobility. Improvements in charge carrier mobility (u_H) might be the consequence of raising the n_H. This means that charge carriers can move more freely inside the material [52].

Table 2: Carrier concentration, mobility, and conductivity of prepared films.

Sample Code	$n\times10^{16}$ (cm^{-3})	μ_H (cm^2/v.sec)	σ_{RT} ($\Omega^{-1}.cm^{-1}$)	Type
PVDF/ PEO	1.92E+17	5.16E+01	1.59E+00	P
0.05 WO_2	3.02E+17	2.44E+02	1.18E+01	P
0.10 WO_2	-2.33E+17	3.38E+01	1.26E+00	N
0.15 WO_2	-7.74E+17	1.78E+01	2.21E+00	N
0.20 WO_2	-1.01E+17	1.05E+02	1.70E+00	N

4. Conclusions

This study successfully employed the spin coating technique to fabricate hybrid PVDF/PEO/WO_2 nanocomposite thin films. X-ray diffraction (XRD) analysis confirmed that the resultant films possessed a polycrystalline structure, a crucial structural feature in materials science. Field emission scanning electron microscopy (FE-SEM) images visually validated the films' microstructure, revealing the presence of hexagonal-like-phase PVDF crystals. Fourier-transform infrared spectroscopy (FTIR) confirmed the characteristics of PVDF/PEO and identified specific doping compounds, confirming successful incorporation. In contrast, PVDF crystals exhibited a fibrous texture akin to tiny fibers. Energy-dispersive X-ray spectroscopy (EDX) analysis offered proof of the successful incorporation of tungsten oxide into the composite matrix. The optical properties supported the tungsten oxide doping-induced augmentation of the optical band gap energy, highlighting the potential uses of these nanocomposite films in sophisticated optoelectronic devices and sensors.

Acknowledgements

The authors would like to thanks University of Baghdad for supporting the research.

Conflict of interest

Authors declare that they have no conflict of interest.

References

1. L. T. White, *Hazardous Gas Monitoring: A Guide for Semiconductor and other Hazardous Occupancies* (UK, William Andrew, 2001).
2. Y. Huang, S. Kormakov, X. He, X. Gao, X. Zheng, Y. Liu, J. Sun, and D. Wu, Polymers **11**, 187 (2019).
3. A. A. Hashim, *Polymer Thin Films* (Rijeca, Croatia, InTechOpen, 2010).
4. L. H. Madkour, *Nanoelectronic Materials: Fundamentals and Applications* (Baljarashi, Suadi Arabia, Springer, 2019).
5. L. W. Mckeen, *Film Properties of Plastics and Elastomers* (Cambridge, US, William Andrew, 2017).

6. M. A. Abed, F. A. Mutlak, A. F. Ahmed, U. M. Nayef, S. K. Abdulridha, and M. S. Jabir, Journal of Physics: Conference Series (Baghdad, Iraq IOP Publishing, 2021). p. 012013.
7. S. S. Khudiar, F. a.-H. Mutlak, and U. M. Nayef, Optik **247**, 167903 (2021).
8. S. S. Khudiar, U. M. Nayef, F. a.-H. Mutlak, and S. K. Abdulridha, Optik **249**, 168300 (2022).
9. X. Wan, H. Cong, G. Jiang, X. Liang, L. Liu, and H. He, ACS Appl. Nano Mat. **6**, 1522 (2023).
10. R. Donate, R. Paz, R. Moriche, M. J. Sayagués, M. E. Alemán-Domínguez, and M. Monzón, Mat. Des. **231**, 112085 (2023).
11. S. Mohammadpourfazeli, S. Arash, A. Ansari, S. Yang, K. Mallick, and R. Bagherzadeh, RSC Advan. **13**, 370 (2023).
12. Z. Feng, Z. Zhao, Y. Liu, Y. Liu, X. Cao, D. G. Yu, and K. Wang, Advan. Mat. Tech. **8**, 2300021 (2023).
13. R. Sun, Q. Tian, M. Li, H. Wang, J. Chang, W. Xu, Z. Li, Y. Pan, F. Wang, and T. Qin, Advan. Funct. Mat. **33**, 2210071 (2023).
14. S. Barrau, A. Ferri, A. Da Costa, J. Defebvin, S. Leroy, R. Desfeux, and J.-M. Lefebvre, ACS Appl. Mat. Interf. **10**, 13092 (2018).
15. V. Caramia, I. S. Bayer, G. C. Anyfantis, R. Ruffilli, F. Ayadi, L. Martiradonna, R. Cingolani, and A. Athanassiou, Nanotechnology **24**, 055602 (2013).
16. Q. M. Al-Bataineh, A. A. Ahmad, A. M. Alsaad, A. Migdadi, and A. Telfah, Phys. B: Conden. Matt. **645**, 414224 (2022).
17. E. Maccaferri, J. Ortolani, L. Mazzocchetti, T. Benelli, T. M. Brugo, A. Zucchelli, and L. Giorgini, ACS Omega **7**, 23189 (2022).
18. M. R. De Campos, A. L. Botelho, and A. C. Dos Reis, Poly. Bull. **80**, 7313 (2023).
19. R. M. N. Javed, A. Al-Othman, M. Tawalbeh, and A. G. Olabi, Renew. Sust. Ener. Rev. **168**, 112836 (2022).
20. M. Batool, M. N. Haider, and T. Javed, J. Inorgan. Organomet. Poly. Mat. **32**, 4478 (2022).
21. C. Pittarate, T. Yoovidhya, W. Srichumpuang, N. Intasanta, and S. Wongsasulak, Poly. J. **43**, 978 (2011).
22. H. M. Hawy and I. M. Ali, Optik **267**, 169659 (2022).
23. H. M. Hawy and I. M. Ali, Optik **262**, 169263 (2022).
24. B. M. Alshabander, Inorg. Nano-Metal Chem. **50**, 1329 (2020).
25. A. A. Salman and A. Al-Janabi, Micro. Opt. Tech. Lett. **62**, 2257 (2020).
26. J. Ramírez-Salgado, R. Quintana-Solórzano, I. Mejía-Centeno, H. Armendáriz-Herrera, A. Rodríguez-Hernández, M. De Lourdes Guzman-Castillo, and J. S. Valente, Appl. Surf. Sci. **573**, 151428 (2022).
27. S. Supothina, P. Seeharaj, S. Yoriya, and M. Sriyudthsak, Ceram. Int. **33**, 931 (2007).
28. J. Gutpa, H. Shaik, K. N. Kumar, and S. A. Sattar, Mat. Sci. Semicond. Proces. **143**, 106534 (2022).
29. M.-U. Nisa, N. Nadeem, M. Yaseen, J. Iqbal, M. Zahid, Q. Abbas, G. Mustafa, and I. Shahid, J. Nanostruct. Chem. **13**, 1 (2022).
30. S. Mujawar, A. Inamdar, S. Patil, and P. Patil, Sol. St. Ion. **177**, 3333 (2006).
31. A. Patterson, Phys. Rev. **56**, 978 (1939).
32. S. M. Al-Jawad, A. A. Taha, and A. M. Redha, J. Sol-Gel Sci. Tech. **91**, 310 (2019).
33. T. Iqbal, M. Irfan, S. M. Ramay, H. M. Gaithan, A. Mahmood, and M. Saleem, Mat. Res. Expr. **6**, 075322 (2019).

34. C. Rameshkumar, S. Sarojini, K. Naresh, and R. Subalakshmi, J. Surf. Sci. Tech. **33**, 12 (2017).
35. A. K. Khaleel and L. K. Abbas, Optik **272**, 170288 (2023).
36. H. Wang, C.-D. Feng, S.-L. Sun, C. U. Segre, and J. R. Stetter, Sens. Actuat. B: Chem. **40**, 211 (1997).
37. S. M. Costa, D. P. Ferreira, A. Ferreira, F. Vaz, and R. Fangueiro, Nanomaterials **8**, 1069 (2018).
38. X. Cai, T. Lei, D. Sun, and L. Lin, RSC Advan. **7**, 15382 (2017).
39. P. Martins, A. Lopes, and S. Lanceros-Mendez, Prog. Poly. Sci. **39**, 683 (2014).
40. Z. Cui, N. T. Hassankiadeh, Y. Zhuang, E. Drioli, and Y. M. Lee, Prog. Poly. Sci. **51**, 94 (2015).
41. F. F. Gondim, L. G. P. Tienne, B. D. S. Macena Da Cruz, E. G. Chaves, A. C. De Carvalho Peres, and M. D. F. V. Marques, J. Appl. Poly. Sci. **138**, 50157 (2021).
42. A. P. Indolia and M. Gaur, J. Poly. Res. **20**, 1 (2013).
43. M. Mohammed, J. Mole. Struct. **1169**, 9 (2018).
44. M. Mohammed, J. Molec. Struct. **1169**, 9 (2018).
45. S. A. Hamdan, Iraqi J. Phys. **17**, 77 (2019).
46. K. A. Aadim and M. M. Shehab .Iraqi J. Phys, 19(49), pp. 42–52 (2021).
47. Z. Li and C. Wang, *One-Dimensional Nanostructures: Electrospinning Technique and Unique Nanofibers* (London, UK, Springer, 2013).
48. S. Pervaiz, N. Kanwal, S. Hussain, M. Saleem, and I. Khan, J. Poly. Res. **28**, 1 (2021).
49. S. Shukla, N. K. Sharma, and V. Sajal, Opt. Quant. Elect. **48**, 1 (2016).
50. N. Narayanan and D. Nk, Mat. Res. **21**, e20180034 (2018).
51. M. Basappa, H. Ganesha, S. Veeresh, Y. Nagaraju, M. Vandana, H. Vijeth, and H. Devendrappa, Chem. Phys. Lett. **799**, 139609 (2022).
52. M. O. Salman, M. A. Kadhim, and A. A. Khalefa, Iraqi J. Sci. **64**, 1190 (2023).

تحضير ودراسة الأغشية الرقيقة الهجينة النانوية PVDF/PEO/WO_2 المحضرة بطريقة الطلاء الدوراني

اسيل نوري بردان[1]، لمياء خضير عباس[1]

[1] قسم الفيزياء، كلية العلوم، جامعة بغداد، بغداد، العراق

الخلاصة

في هذه الدراسة، نستكشف تأثير تطعيم أكسيد التنكستن النانوي (WO_2) على أغشية فلوريد البولي فينيل (PVDF)/ أكسيد البولي ايثيلين (PEO) الرقيقة، المُصنعة باستخدام تقنية الطلاء بالدوران. الابتكار في هذا البحث يتجلى في استقصاء نسب الوزن المختلفة لجسيمات WO_2 النانوية داخل أفلام المركبة. تم استخدام تقنيات شاملة للتوصيف، بما في ذلك التحليل الهيكلي من خلال تقنية حيود الأشعة السينية (XRD)، والتي أظهرت الطبيعة البلورية للأفلام بهياكل رباعية الشكل وزيادة ملحوظة في حجم الحبيبات مع زيادة نسبة وزن جسيمات WO_2. أما فحوصات المجهر الإلكتروني الماسح للانبعاثات الميدانية (FE-SEM) فقد أظهرت توزيعاً متجانساً لجسيمات WO_2 النانوية، وهو إنجاز حاسم. علاوة على ذلك، أكد تحليل تحويل فورييه لطيف الأشعة تحت الحمراء (FTIR) تركيب المركبات المطعمة بنجاح. كشف تحليل نفاذية الضوء عن فجوة الطاقة البصرية للأفلام، وأنواع الانتقال البصري، وخصائص الامتصاص البصري، حيث يتجلى الابتكار عندما تزيد فجوة الطاقة البصرية بشكل كبير من 3.0 إلكترون فولت إلى 3.64 إلكترون فولت مع زيادة نسبة وزن جسيمات WO_2، مما يشير إلى تعديلات هيكلية إلكترونية عميقة وإمكانيات تطبيقية في مجالات الأشباه الموصلات والأجهزة البصرية.

الكلمات المفتاحية: فلوريد البولي فينيل/ أكسيد البولي ايثيلين، المتراكبات النانوية، الطلاء المغزلي، متعدد البلورات، المجهر الإلكتروني الماسح للانبعاثات الميدانية.